

Influence of Boundary Conditions on Oscillatory Flow in a Grooved Channel

Takuya Masuda¹, Miah Md Ashraful Alam², Tatsuki Hamada¹, Masaki Sakaguchi¹, Takatoshi Fujii¹, Yasutaka Hayamizu¹

¹Department of Integrated Engineering, National Institute of Technology, Yonago College, Tottori, Japan

²Department of Systems Engineering, Osaka Sangyo University, Osaka, Japan

Email: masuda@yonago-k.ac.jp

How to cite this paper: Masuda, T., Alam, M.M.A., Hamada, T., Sakaguchi, M., Fujii, T. and Hayamizu, Y. (2025) Influence of Boundary Conditions on Oscillatory Flow in a Grooved Channel. *Open Journal of Fluid Dynamics*, 15, 116-131.

<https://doi.org/10.4236/ojfd.2025.152007>

Received: May 13, 2025

Accepted: June 16, 2025

Published: June 19, 2025

Copyright © 2025 by author(s) and Scientific Research Publishing Inc. This work is licensed under the Creative Commons Attribution International License (CC BY 4.0).

<http://creativecommons.org/licenses/by/4.0/>



Open Access

Abstract

In this study, a numerical analysis was performed to simulate the flow in a grooved channel with a periodic boundary condition in the main flow direction, and three-dimensional oscillatory flow was obtained. The influence of different streamwise boundary conditions was examined by comparing with previous experimental results. Furthermore, the impact of spanwise boundary conditions—either wall or periodic—on the flow characteristics was investigated. Under the wall boundary condition, as the Reynolds number increases, the flow transitions from symmetric three-dimensional oscillatory flow to asymmetric three-dimensional oscillatory flow. Under the periodic boundary condition, the flow evolves from two-dimensional oscillatory flow to symmetric three-dimensional oscillatory flow, and eventually to asymmetric three-dimensional oscillatory flow. As the Reynolds number increases, the waveform of the time-evolving velocity component changes from a simple sinusoidal wave to one accompanied by long-period undulations, followed by irregular short-period oscillations, and finally, the amplitude spectrum no longer shows a distinct fundamental frequency. Vortex structures evolve from spanwise-elongated shapes to massive vortex clusters, which further subdivide into finer structures. The time-averaged wall shear stress at the center of the channel exhibits the largest discrepancy from experimental results around a Reynolds number of 548, which is attributed to long-period flow undulations. However, no significant difference in wall shear stress was observed between wall and periodic boundary conditions.

Keywords

Transition, CFD, Finite Volume Method, Three-Dimensional Flow, Wall Shear Stress

1. Introduction

The flow within a channel with grooves in the middle of parallel plates transitions from a steady flow to a self-sustained oscillatory flow when the Reynolds number exceeds a certain threshold. It is believed that this oscillatory flow is triggered by Kelvin-Helmholtz instability in the groove regions [1], which enhances heat and mass mixing.

Grooved channels are used in various applications, such as fluid machinery and chemical plants. Examples of their use in the laminar flow regime include injection molding dies and the etching process of printed circuit boards. Recently, attention has been drawn to transport phenomena in the laminar flow regime, particularly for applications in biomedical engineering, such as small-scale analytical devices and artificial organs. Additionally, oscillatory flows in grooved channels are relevant in the design of microfluidic mixers [2], heat exchangers [3], and bioreactors [4], where enhanced mass and momentum transfer under laminar conditions is desired. Understanding the effects of boundary conditions can aid in optimizing such systems for improved performance.

Nishimura *et al.* [5] [6] conducted experiments using channels with grooves on one side to visualize flow patterns and measure wall shear stress and mass transfer rates. The channel used in their experiments had eight grooves, with the fifth groove from the upstream side being the focus of measurements. At low Reynolds numbers, the flow was steady, transitioning to two-dimensional oscillatory flow at $Re > 300$ in the central part of the channel, and developing into three-dimensional oscillatory flow at $Re > 450$. In the three-dimensional oscillatory flow, stripe patterns along the main flow direction were observed. These stripe intervals became narrower with increasing Reynolds number and appeared to revert to two-dimensional oscillatory flow. This phenomenon was described in previous studies as “quasi-two-dimensional flow”.

Regarding past numerical simulations for channels with the same geometry as the aforementioned experiments, studies have computed two-dimensional steady and oscillatory flows [5] [6], three-dimensional steady flows [7], and three-dimensional oscillatory flows just after the onset of self-sustained oscillations [8]. However, oscillatory flows exhibiting fully developed three-dimensionality in the central part of the channel have not yet been reported.

For channels with grooves on both sides, it is known through two-dimensional numerical analysis and experiments that the flow transitions from steady to periodic oscillatory flow [9]. While periodic boundary conditions in the main flow direction are often applied in numerical simulations, inflow and outflow boundary conditions mimicking experimental setups have also been studied. The critical Reynolds number for the transition to oscillatory flow differs between these two conditions [10] [11]. Additionally, the critical Reynolds number varies with the number of grooves [12].

Numerical simulations of flows between parallel plates often employ periodic boundary conditions in the spanwise direction [13]. However, experimental setups inevitably involve walls in the spanwise direction, imposing wall boundary condi-

tions. Experiments on flows between parallel plates have used sufficiently wide rectangular channels to measure flows away from the spanwise sidewalls [14]. In grooved channels, however, spanwise vortical flows directed from the sidewalls toward the channel center exist [7]. Therefore, even when three-dimensionality in the central part of the channel is fully developed, the characteristics of three-dimensional oscillatory flows may not necessarily match under wall boundary conditions and periodic boundary conditions.

In this study, we reproduced the experiments of [5] [6] through three-dimensional numerical simulations to obtain flow patterns and vortex structures. By comparing the results with experiments using inflow and outflow boundary conditions under periodic boundary conditions in the main flow direction, we examined the impact of these differences on the flow. Furthermore, we investigated the influence of spanwise boundary conditions between the wall and periodic boundary conditions.

2. Methods

2.1. Governing Equations and Channels

This study focuses on incompressible viscous fluid flow. The governing equations are the dimensionless continuity Equation (1) and the Navier-Stokes Equation (2), with viscous dissipation neglected.

$$\nabla \cdot \mathbf{u} = 0 \quad (1)$$

$$\frac{\partial \mathbf{u}}{\partial t} + \nabla \cdot (\mathbf{u}\mathbf{u}) = -\nabla p + \frac{1}{Re} \nabla^2 \mathbf{u} \quad (2)$$

Here, dimensional quantities are represented using an asterisk (*), and the equations are non-dimensionalized as $t = t^* U^* / H^*$, $\mathbf{x} = \mathbf{x}^* / H^*$, $p = p^* / (\rho U^{*2})$, $\mathbf{u} = \mathbf{u}^* / U^*$.

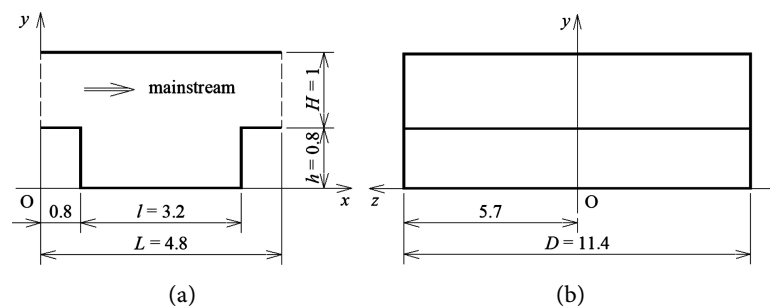


Figure 1. Configuration of the channel and coordinate system. (a) Side view, (b) Front view.

Figure 1 shows the channel geometry and coordinate system. The left diagram is the front view, and the right diagram is the side view. The channel features a rectangular groove on the central lower side of the parallel plates. Using the origin O as a reference, a right-handed Cartesian coordinate system is defined. The x -axis lies along the centerline of the groove's bottom, the y -axis is normal to the

parallel plates intersecting the x -axis at the left end of the channel, and the z -axis is along the spanwise direction. The main flow is assumed to be along the x -axis.

The channel geometry is approximately the same as those used in the experiments [5] and three-dimensional simulations [7]. The channel's total length is $L = 4.8$, the channel height in the no grooved region is $H = 1$, and the depth is $D = 11.4$. The groove length and height are set to $l = 3.2$ and $h = 0.8$, respectively.

Periodic boundary conditions expressed by Equation (3) were imposed in the main flow direction, along with a constant flow rate condition:

$$\begin{aligned} \mathbf{u}(x+L, y, z, t) &= \mathbf{u}(x, y, z, t), \\ p(x+L, y, z, t) &= p(x, y, z, t) - \Delta p. \end{aligned} \quad (3)$$

Here, Δp represents the mean pressure drop. A fixed pressure of $p = 0$ was set at the point $(x, y, z) = (4.8, 1.3, 0)$.

Boundary conditions at both ends in the spanwise direction included three types: 1) wall boundary conditions, 2) periodic boundary conditions, and 3) two-dimensional conditions. The periodic boundary conditions in the spanwise direction are defined by Equation (4):

$$\begin{aligned} \mathbf{u}(x, y, z+D/2, t) &= \mathbf{u}(x, y, z-D/2, t), \\ p(x, y, z+D/2, t) &= p(x, y, z-D/2, t). \end{aligned} \quad (4)$$

For wall boundary conditions, the velocity \mathbf{u} was set to a no-slip condition, and the pressure p was specified to have a zero normal gradient. The remaining boundary surfaces also employed these wall boundary conditions. In two-dimensional conditions, physical quantities are assumed to be invariant in the z -direction.

2.2. Numerical Solutions

In this study, the open-source software OpenFOAM 3.0.1 was used to discretize the governing equations with the finite volume method and perform unsteady numerical simulations [15] [16]. The application of this software to three-dimensional flows in sudden expansion channels within the transitional regime has been previously reported [17]-[19].

The numerical scheme employed a second-order Crank-Nicholson method for time integration and second-order central differences for advection, viscous, and pressure terms, ensuring overall second-order accuracy. The PIMPLE algorithm, which combines the PISO and SIMPLE methods, was used for pressure-velocity coupling. The solvers applied were the geometric-algebraic multi-grid (GAMG) method for pressure and the Gauss-Seidel method for velocity. Iterative calculations continued until the residuals of velocity divergence decreased to 10^{-10} . Although OpenFOAM allows for the use of various iterative solvers, we have confirmed that while the choice of solver may affect computational time, it does not influence the simulation results themselves.

As shown in **Figure 2**, a non-uniform mesh with dense spacing near walls was employed for discretization. Three types of meshes were prepared for cases with wall boundary conditions in the spanwise direction. The number of mesh elements was $31 \times 22 \times 108$ for Model A, $42 \times 30 \times 108$ for Model B, and $42 \times 30 \times 153$ for Model C. **Figure 2** illustrates Model C. These mesh configurations were determined based on previous calculations for steady flows [7], with Model B being the closest to those used in prior studies. The non-uniform mesh had a maximum-to-minimum spacing ratio of 8, with spacing changing geometrically. For cases with periodic boundary conditions in the spanwise direction, the mesh was uniform in the spanwise direction, with a configuration equivalent to $42 \times 30 \times 137$ for Model C. For two-dimensional conditions, the mesh configuration was 42×30 , equivalent to Model C.

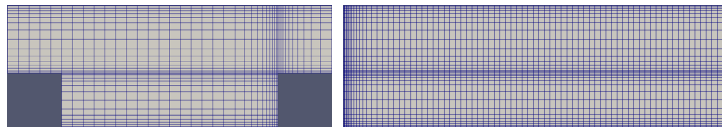


Figure 2. Structure of the mesh system in Model C.

The time step was set to $\Delta t = 0.002$ to maintain a maximum Courant number of $Co_{\max} \approx 0.2$. **Figure 9** compares the distribution of the time-averaged velocity component $\langle u \rangle$ at $Re = 350$ and $Re = 658$ using the three different mesh models. No qualitative differences were observed in the flow characteristics due to the variation in mesh resolution. Since the flow patterns did not vary significantly among the three mesh types, the results obtained with Model C are presented unless otherwise noted.

3. Results and Discussion

3.1. Flow Patterns and Vortex Structures

The flow patterns are classified into four types: two-dimensional steady flow (A), two-dimensional oscillatory flow (B), three-dimensional steady flow (C), and three-dimensional oscillatory flow (D). The three-dimensional steady flow is observed only under wall boundary conditions and is symmetric in the xy -plane at $z = 0$. Three-dimensional oscillatory flows are further categorized into symmetric flows (D.1), where $w = 0$ in any xy -plane, and asymmetric flows (D.2), where $w \neq 0$ in all xy -planes. The flow symmetry in any xy -plane is expressed by Equation (5):

$$\begin{aligned} u(+z) &= u(-z), v(+z) = v(-z), \\ w(+z) &= w(-z), p(+z) = p(-z). \end{aligned} \quad (5)$$

Here, “any xy -plane” refers to the xy -plane at $z = 0$ for wall boundary conditions, while it includes all xy -planes at any z for periodic boundary conditions.

Figure 3 shows the distribution of the velocity component w along a line at z -axis for $(x, y) = (3.2, 0.4)$. At a given moment, it is used to examine the symmetry

in the xy -plane. The moment when w is presumed to have the largest amplitude was selected visually. Below, the changes in symmetry with respect to spanwise boundary conditions and Reynolds numbers Re are described.

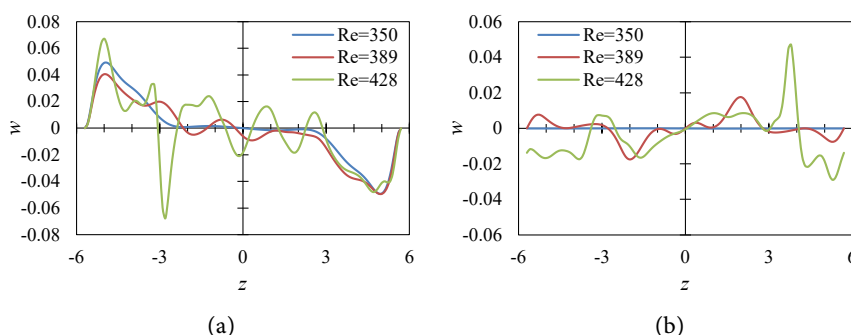


Figure 3. An instantaneous distribution of the velocity component w along a line of $(x, y) = (3.2, 0.4)$ for $-5.7 \leq z \leq 5.7$. (a) Wall boundary, (b) Periodic boundary.

Under wall boundary conditions, at $Re = 350$, the flow is symmetric with $w = 0$ at $z = 0$, but the symmetry is lost at $Re \geq 389$. For periodic boundary conditions, at $Re = 350$, the flow is two-dimensional with $w = 0$ at all z . At $Re = 389$, the flow is three-dimensional symmetric with $w = 0$ at $z = 0$. For $Re \geq 428$, the flow becomes asymmetric with $w \neq 0$ in all xy -planes. The symmetric center at $z = 0$ for $Re = 389$ under periodic boundary conditions resulted from computational constraints, as the computational domain is symmetric at $z = 0$ and the relative pressure $p = 0$ is defined at $(x, y, z) = (4.8, 1.3, 0)$.

Figure 4 shows the time evolution of the velocity component w at $(x, y, z) = (3.2, 0.4, 0)$ and $(3.2, 0.4, 5.2)$. Combined with the symmetry results in **Figure 3**, the flow patterns are examined with respect to differences in spanwise boundary conditions and Reynolds number Re .

At $Re = 300$, the flow is steady regardless of spanwise boundary conditions. Under wall boundary conditions, at $Re = 350$, the flow is a symmetric three-dimensional oscillatory flow with $w = 0$ in the xy -plane at $z = 0$. At $Re = 389$, the flow transitions to an asymmetric three-dimensional oscillatory flow with $w \neq 0$ at $z = 0$. The dominant oscillatory component appears to be a simple sinusoidal wave but includes long-period undulations. At $Re = 428$, the undulations intensify, and short-period irregular fluctuations emerge. These irregular oscillations become more pronounced at $Re = 548$ and $Re = 658$.

Under periodic boundary conditions, at $Re = 350$, the waveform is a simple sinusoidal wave, and the flow remains two-dimensional with $w = 0$ across all z . At $Re = 389$, the oscillatory flow includes long-period undulations; $w = 0$ at $z = 0$, but oscillations with $w \neq 0$ are observed at $z = 5.2$, indicating a symmetric three-dimensional oscillatory flow in the xy -plane at $z = 0$. For $Re \geq 428$, $w \neq 0$ at $z = 0$, and the flow transitions to an asymmetric three-dimensional oscillatory flow across all xy -planes, similar to the characteristics under wall boundary conditions.

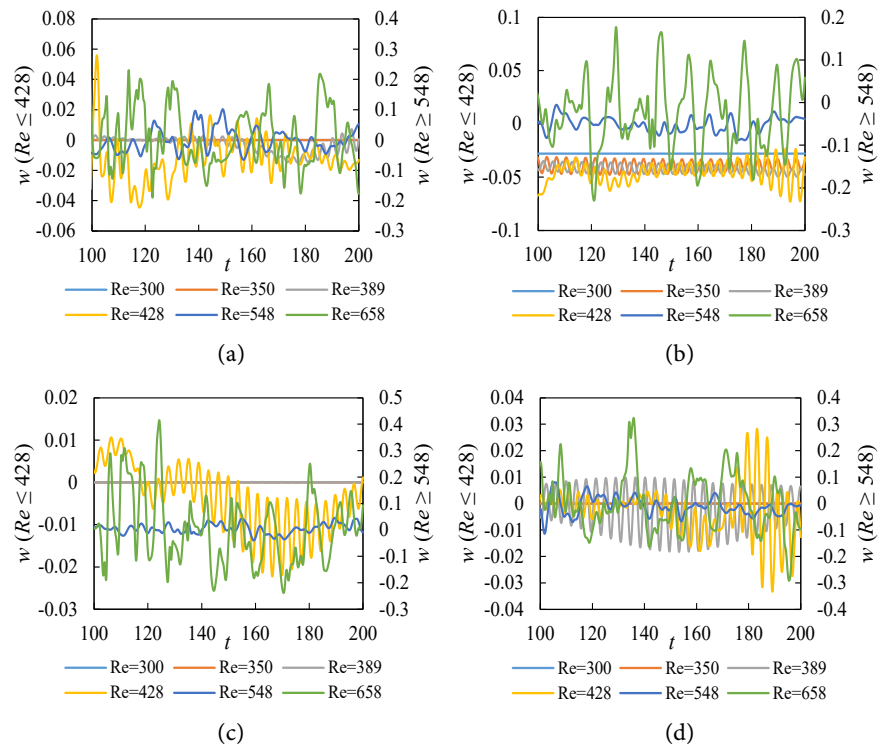


Figure 4. Effect of the sidewall condition on the evolution of the velocity component w at two different points. (a) $(x, y, z) = (3.2, 0.4, 0)$, wall boundary, (b) $(x, y, z) = (3.2, 0.4, 5.2)$, wall boundary, (c) $(x, y, z) = (3.2, 0.4, 0)$, periodic boundary, (d) $(x, y, z) = (3.2, 0.4, 5.2)$, periodic boundary.

These characteristics are confirmed to apply throughout the channel by visualizing vortex structures, as shown later in **Figure 7**. For two-dimensional calculations, simple sinusoidal waves are obtained for all cases with $Re > 300$.

Figure 5 illustrates the time evolution of the velocity component v at $(x, y, z) = (3.2, 0.4, 0)$. The waveform shows a simple sinusoidal pattern at $Re = 350$, long-period undulations at $Re = 389$, and both long-period undulations and short-period irregular fluctuations at $Re \geq 428$.

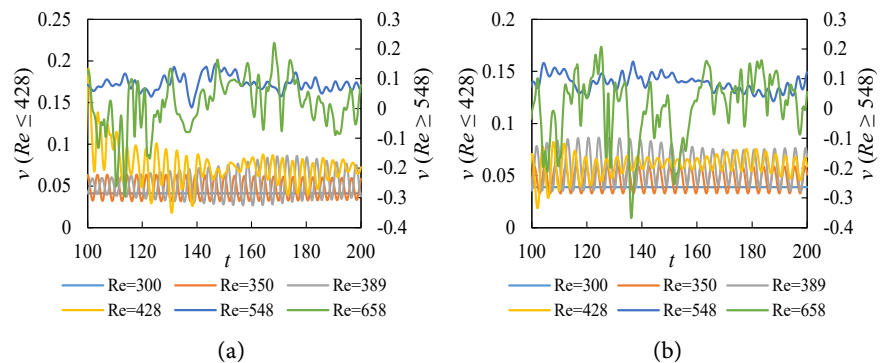


Figure 5. Effect of the sidewall condition on the evolution of the velocity component v at $(x, y, z) = (3.2, 0.4, 0)$. (a) Wall boundary, (b) Periodic boundary.

Figure 6 shows the amplitude spectrum $|V(St)|$ of the velocity component v at $(x, y, z) = (3.2, 0.4, 0)$. The time-series data shown in **Figure 5** were analyzed for frequency characteristics using a fast Fourier transform (FFT). In previous two-dimensional simulations, $St = 0.306$ was obtained regardless of Re , and experimental results for $Re < 550$ showed St values within the range of -10% to $+5\%$ relative to the two-dimensional simulation results, mostly concentrated in the range of -5% to 0% [5]. The oscillation characteristics were examined in conjunction with the time-series waveforms shown in **Figure 5**.

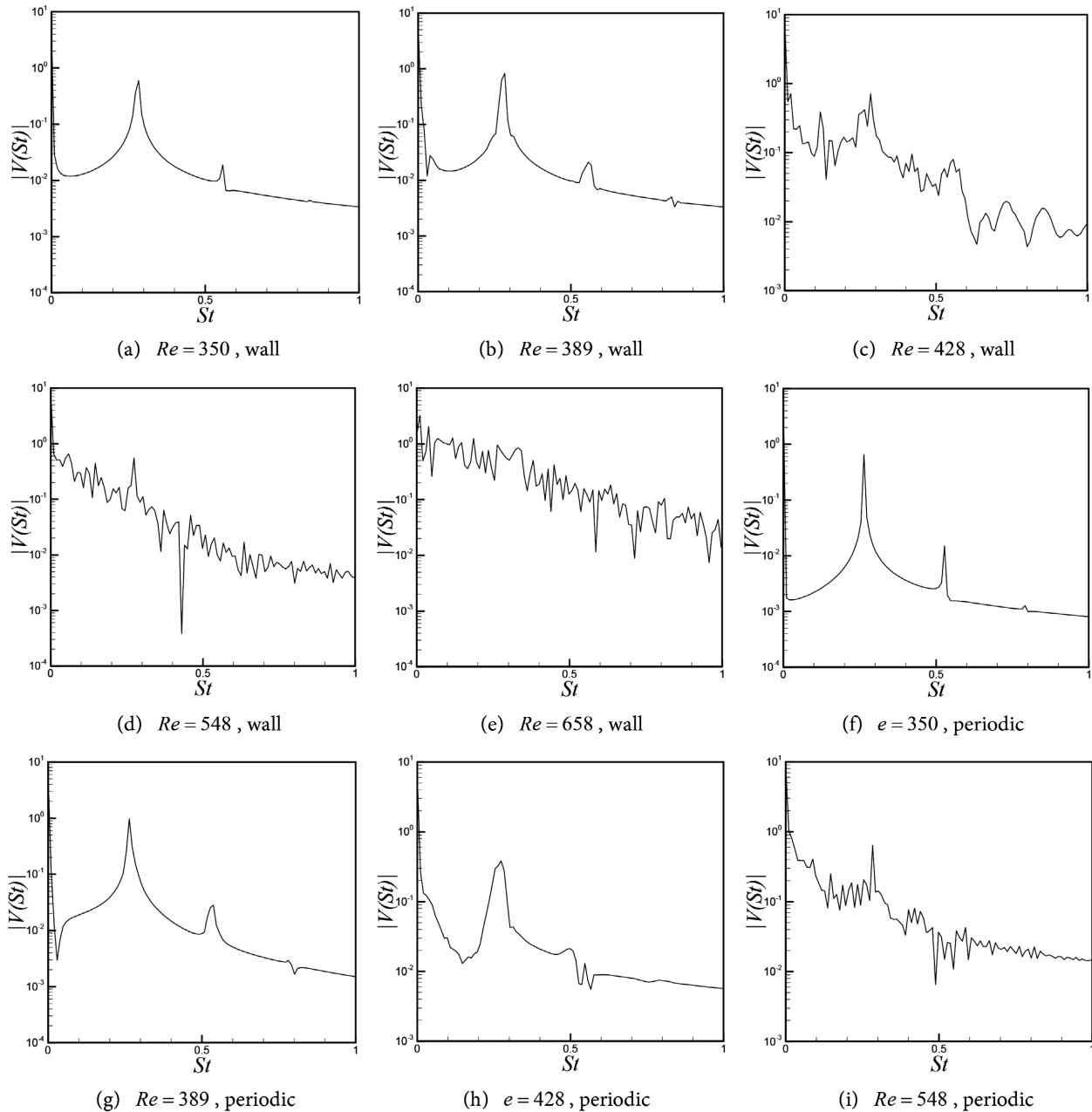


Figure 6. Amplitude spectrum $|V(St)|$ of the velocity component v at $(x, y, z) = (3.2, 0.4, 0)$ as a function of Strouhal number St .

First, the results for wall boundary conditions are discussed:

1) At $Re = 350$, only the peaks of the fundamental wave and its harmonics were observed.

2) At $Re = 389$, the amplitude spectrum exhibited a similar distribution to $Re = 350$. However, a small peak appeared at $St = 0.0488$ due to the long-period undulations shown in **Figure 5**.

3) At $Re = 428$, the peaks of the fundamental wave and its harmonics were clearly identifiable, but non-periodic components also emerged.

4) At $Re = 548$, the proportion of non-periodic components further increased, although the peak of the fundamental wave remained distinguishable.

5) At $Re = 658$, the peak of the fundamental wave could no longer be identified in the amplitude spectrum. The fundamental St was $St = 0.283$ for $Re = 350$ to 428 and $St = 0.273$ for $Re = 548$.

Next, the results for periodic boundary conditions are discussed:

6) At $Re = 350$, only the peaks of the fundamental wave and its harmonics were observed.

7) At $Re = 389$, long-period undulations occurred, as shown in **Figure 5**, but no peaks were observed in the amplitude spectrum.

8) At $Re = 428$, similar trends to $Re = 389$ were observed.

9) At $Re = 548$, non-periodic components appeared alongside the fundamental wave and its first harmonic, whose peaks were distinguishable.

At $Re = 658$, the distribution resembled that under wall boundary conditions, and the peak of the fundamental wave could no longer be identified in the amplitude spectrum. The fundamental St values were $St = 0.264$ for $Re = 350$ and $Re = 389$, $St = 0.273$ for $Re = 428$, and $St = 0.283$ for $Re = 548$.

Figure 7 shows an iso-surface of the second invariant of the velocity gradient tensor Q at a given moment, with the flow moving from the top left to the bottom right. Q , is defined by Equation (6):

$$Q = -\frac{1}{2} \frac{\partial u_i}{\partial x_j} \frac{\partial u_j}{\partial x_i} \quad (i, j = 1, 2, 3). \quad (6)$$

Regions where $Q > 0$ are defined as vortex regions. The selection of Q -isosurfaces is arbitrary, and $Q = 0$ is unsuitable for visualizing vortex structures as it encompasses most of the domain. In this study, the values were visually adjusted to ensure the enclosed volume by the isosurface accounted for 5% of the total volume, using the range $0.2 \leq Q \leq 1.5$.

Common features across all conditions include the generation of elongated vortices in the spanwise direction, wrapping around the downstream corners. The maximum Q values were observed at the vortex core, exceeding 1000 for $Re = 658$. Results for wall boundary conditions are as follows:

1) At $Re = 350$, vortices stretched thinly in the spanwise direction and were symmetric in the xy -plane at $z = 0$.

2) At $Re = 389$, similar thin, elongated vortices were observed, but they exhibited asymmetric vortex structures.

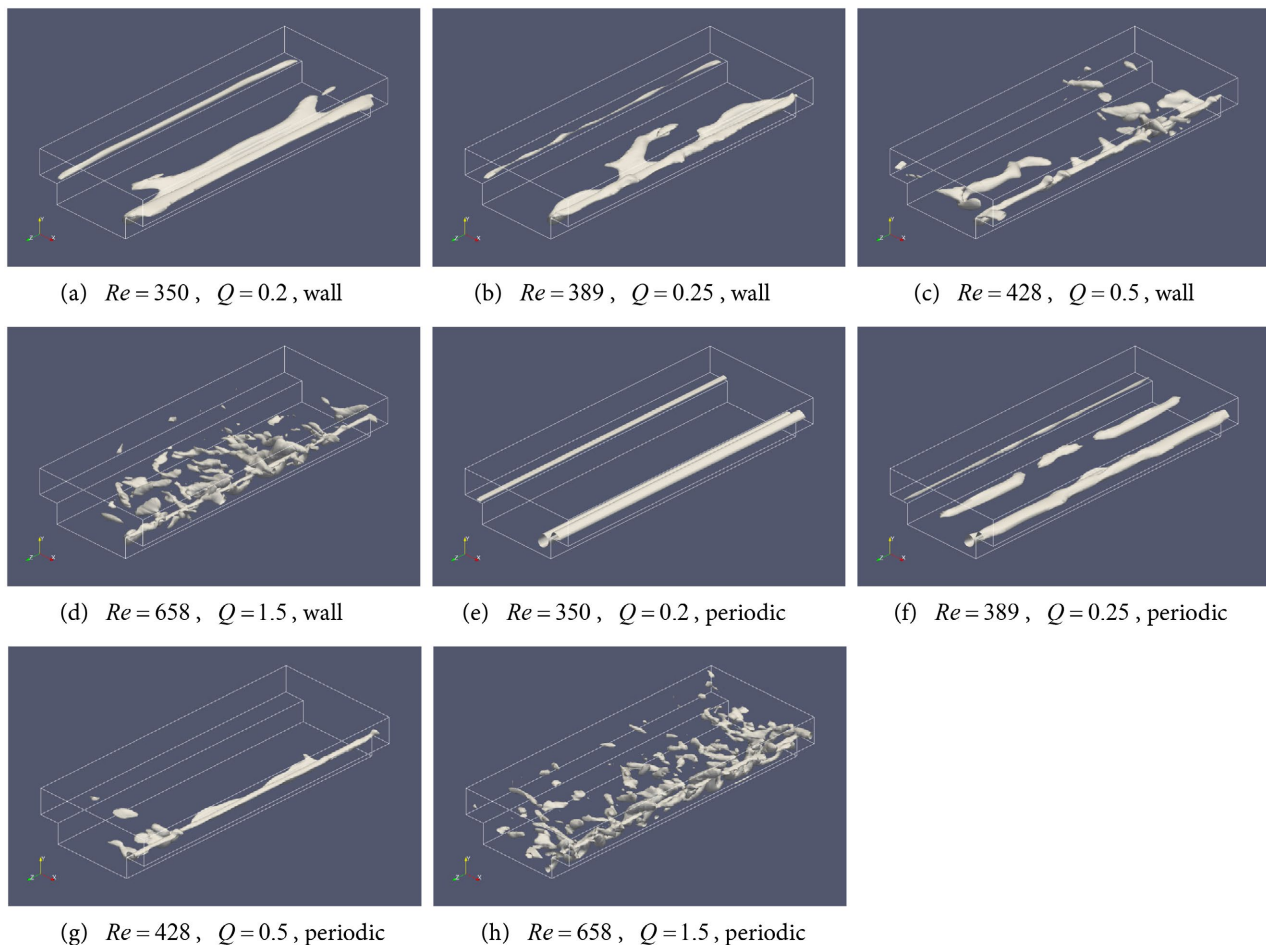


Figure 7. Iso-surface of second invariant Q of velocity gradient tensor.

3) At $Re = 428$, in addition to elongated vortices wrapping around the downstream corners, multiple vortices of varying sizes were identified.

At $Re = 548$, these vortices became smaller and more numerous.

4) At $Re = 658$, the vortices became further subdivided.

For periodic boundary conditions, the same Q -isosurfaces were used:

5) At $Re = 350$, uniformly elongated vortices appeared in the spanwise direction.

6) At $Re = 389$, spanwise symmetry was maintained in the xy -plane at $z = 0$.

7) At $Re = 428$, asymmetry developed in the spanwise direction, with localized vortex clusters.

8) At $Re = 548$ and $Re = 658$, vortex structures became further subdivided, similar to those under wall boundary conditions.

In summary, as Re increases, the flow transitions as follows:

- In two-dimensional space: (A) two-dimensional steady flow \rightarrow (B) two-dimensional oscillatory flow.
- Under wall boundary conditions: (C) three-dimensional steady flow \rightarrow (D.1) three-dimensional symmetric oscillatory flow in the xy -plane at $z = 0 \rightarrow$

(D.2) three-dimensional asymmetric oscillatory flow in all xy -planes.

- Under periodic boundary conditions: (A) two-dimensional steady flow \rightarrow (B) two-dimensional oscillatory flow \rightarrow (D.1) three-dimensional symmetric oscillatory flow in any xy -plane \rightarrow (D.2) three-dimensional asymmetric oscillatory flow in all xy -planes.

For both wall and periodic boundary conditions, the flow transitions to asymmetric three-dimensional oscillatory flow at $Re \geq 428$.

3.2. Time Averaging and Comparison with Experimental Results

When oscillations involve low- St undulations, the timing of the time-averaging operation affects the averaged values. **Figure 8** shows the time-averaged velocity component $\langle u \rangle$ and the root mean square (RMS) of the fluctuating velocity component u' (u'_{RMS}) for every 100 dimensionless time units at $Re = 658$. Data were collected at $(x, y, z) = (2.4, 1.3, 0)$, corresponding to the centerline in the y -direction of the ungrooved region of the channel. Model A was used for the mesh, and data were collected at intervals of 0.1 dimensionless time over 500 dimensionless time units. When the averaging range is $t = 0$ to T , $\langle u \rangle$ and u'_{RMS} are defined by Equations (7) and (8):

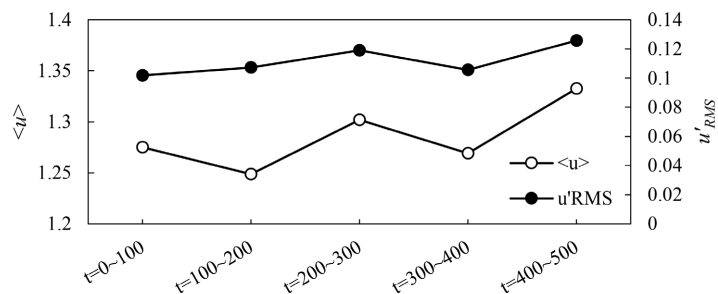


Figure 8. Time-averaged velocity component $\langle u \rangle$ and RMS of time-varying velocity component u'_{RMS} for every 100 dimensionless times at $Re = 658$. The data for 500 dimensionless times at $(x, y, z) = (2.4, 1.3, 0)$ were used with the mesh system of Model A.

$$\langle u \rangle = \frac{1}{T} \int_0^T u dt \quad (7)$$

$$u'_{\text{RMS}} = \sqrt{\langle u'^2 \rangle} = \sqrt{\frac{1}{T} \int_0^T u'^2 dt} \quad (8)$$

The same definitions were applied to velocity components v , w , and wall shear stress τ_0 for time-averaging. The errors, assuming the median values as true values, were $\pm 4.47\%$ for $\langle u \rangle$ and $\pm 14.0\%$ for u'_{RMS} . Similarly, errors for v'_{RMS} and w'_{RMS} were $\pm 4.31\%$ and $\pm 5.69\%$, respectively. Subsequent discussions consider that the time-averaged velocity components and the RMS of fluctuating components include errors within these ranges. Unless otherwise noted, time-averaging was conducted using results over 100 dimensionless time units. In dimensional terms, based on the channel geometry and fluid properties used in the exper-

iment [20], 100 dimensionless time units correspond to 7.09 seconds at $Re = 658$.

Figure 9 shows the distribution of $\langle u \rangle$ along the y -axis at $x = 2.4$ and $z = 0$. As seen from **Figure 9(a)**, at $Re = 350$, $\langle u \rangle$ reached a maximum at $y = 1.3$, the heightwise centerline of the ungrooved region. This maximum value is denoted as $\langle u \rangle_{\max}$. Under wall boundary conditions using Model C, $\langle u \rangle_{\max} = 1.47$. Comparing errors among different meshes, $\langle u \rangle_{\max}$ obtained with Model A and Model B showed errors of -1.09% and $+0.31\%$, respectively, relative to Model C. Under periodic boundary conditions and two-dimensional conditions, $\langle u \rangle_{\max}$ was -4.86% and -4.87% , respectively, compared to Model C. This indicates that the time-averaged maximum velocity in the main flow direction under wall boundary conditions is higher than that under periodic or two-dimensional conditions, consistent with previous reports for steady flows [7]. While at $Re = 658$, as shown in **Figure 9(b)**, variations in the time-averaged components increased due to the timing of the averaging under both wall and periodic boundary conditions. The location of y where $\langle u \rangle_{\max}$ occurs became indeterminate but was confirmed to be within the range $1.25 < y < 1.45$ in this study. Qualitatively, at $Re = 658$, the faster main flow was observed to sink into the grooved regions compared to $Re = 350$.

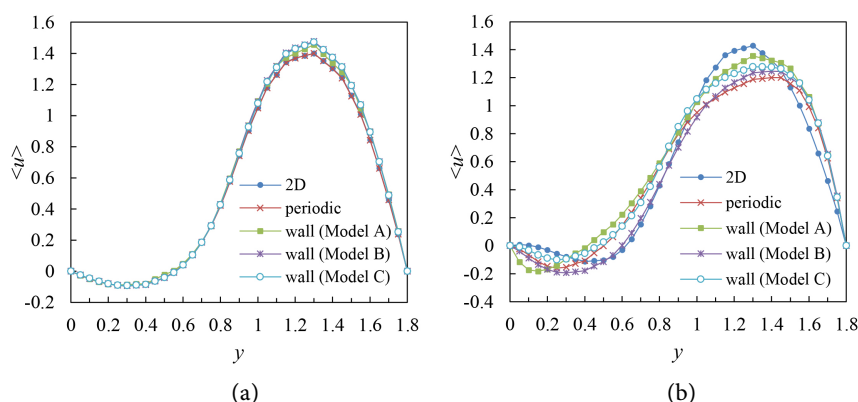


Figure 9. Distribution of the time-averaged velocity component $\langle u \rangle$ on a line along the y -axis at $(x, z) = (2.4, 0)$. (a) $Re = 350$, (b) $Re = 658$.

Figure 10 shows the distribution of the time-averaged absolute wall shear stress $\langle |\tau_0| \rangle$. Data were collected at two points, A $(x, y, z) = (4.8, 0.8, 0)$ and B $(x, y, z) = (4.0, 0.4, 0)$, corresponding to nearly the same locations as in the experiment [3]. Both the simulation and experimental results are presented in dimensionless form in **Figure 10**. Wall shear stress was non-dimensionalized as $\tau_0 = \tau_0^* / (\rho U^{*2})$. The value of $\langle |\tau_0| \rangle$, like velocity, varied depending on the timing of the time-averaging operation. Using the same procedure as shown in **Figure 8**, the variation of $\langle |\tau_0| \rangle$ for every 100 dimensionless time units was examined at $Re = 658$ using Model A. The maximum and minimum values at point A were $\langle |\tau_0| \rangle_{\max} = 0.0153$ and $\langle |\tau_0| \rangle_{\min} = 0.0110$, respectively, while at point B, they were $\langle |\tau_0| \rangle_{\max} = 0.0188$ and $\langle |\tau_0| \rangle_{\min} = 0.0135$. The errors relative to the median

values were $\pm 10.2\%$ at point A and $\pm 7.9\%$ at point B.

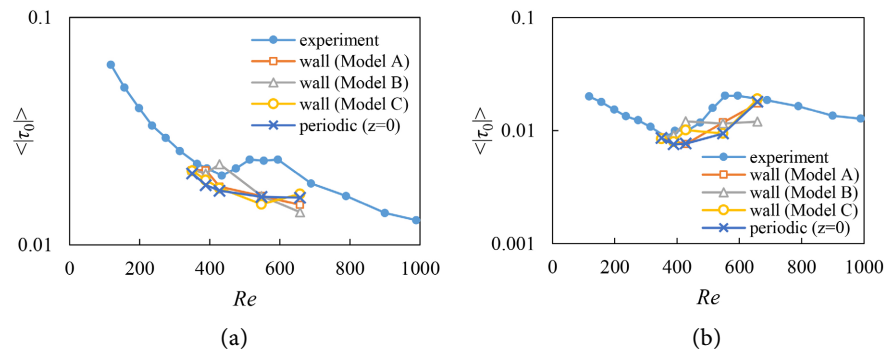


Figure 10. Time-averaged absolute value of dimensionless wall shear stress $\langle \tau_0 \rangle$ as a function of the Reynolds number Re . The data were acquired at the two places: point A $(x, y, z) = (4.8, 0.8, 0)$ and point B $(x, y, z) = (4, 0.4, 0)$. Those points are the same places as the experiment [6]. (a) Point A, (b) Point B.

For $\langle |\tau_0| \rangle$ computed under the four conditions (Model A, Model B, Model C, and periodic boundary conditions), the errors relative to the median values at points A and B were $\pm 26.6\%$ and $\pm 35.9\%$ at $Re = 428$, and a maximum of $\pm 7.58\%$ and $\pm 12.9\%$ for other Re . The discrepancy in $\langle |\tau_0| \rangle$ for $Re = 428$ obtained with Model B compared to other meshes and boundary conditions is attributed to the occurrence of particularly large undulations by chance. As shown in the Q -isosurfaces in Figure 7, localized vortex clusters emerge at $Re = 428$, making the time-averaged values prone to greater variability. At $Re = 548$, the fluctuation amplitude is significantly affected by low-frequency undulations, resulting in a greater sensitivity of time-averaged values to the duration and phase of sampling. This sensitivity amplifies the discrepancies among different mesh models.

When comparing the simulation results with experimental data, significant differences were observed at $Re = 548$ in the channel center at $z = 0$. However, no notable differences in $\langle |\tau_0| \rangle$ were observed between wall boundary conditions and periodic boundary conditions.

The time-averaged wall shear stress values at two representative points in the channel were compared with the experimental data from Nishimura *et al.* [6]. Overall, good agreement was observed across a wide range of Reynolds numbers, except at $Re = 548$, where low-frequency undulations resulted in larger variability. These comparisons validate the numerical approach used in this study.

4. Conclusions

In this study, numerical simulations were conducted on the flow within a grooved channel under periodic boundary conditions in the main flow direction, reproducing three-dimensional oscillatory flow. The results were compared with experimental data to investigate the impact of differences in boundary conditions. Based on the oscillatory flow observed in the channel for $350 \leq Re \leq 658$, the following conclusions were obtained:

1) Under wall boundary conditions, at $Re = 350$, the flow was a symmetric three-dimensional oscillatory flow with $w = 0$ in the xy -plane at $z = 0$. At $Re \geq 389$, the flow transitioned to an asymmetric three-dimensional oscillatory flow in the xy -plane at $z = 0$. Under periodic boundary conditions, the flow was a two-dimensional oscillatory flow at $Re = 350$, transitioned to a symmetric three-dimensional oscillatory flow in any xy -plane at $Re = 389$, and became asymmetric in all xy -planes at $Re \geq 428$.

2) The time evolution of velocity components exhibited a simple sinusoidal waveform at $Re = 350$, included long-period undulations at $Re = 389$, and displayed both long-period undulations and short-period irregular fluctuations at $Re \geq 428$. At $Re = 658$, the fundamental wave could no longer be identified in the amplitude spectrum. Vortex structures evolved with increasing Re , changing from spanwise elongated forms to vortex clusters and further subdividing into smaller structures.

3) For the time-averaged absolute value of wall shear stress $\langle |\tau_0| \rangle$ at the channel center ($z = 0$), the largest discrepancies between numerical and experimental results were observed around $Re = 548$. However, no significant differences in $\langle |\tau_0| \rangle$ were found between wall and periodic boundary conditions. The significant deviation in wall shear stress at $Re = 548$ is attributed to the sensitivity of time-averaged quantities to long-period flow undulations and the resulting mesh-to-mesh variability.

The analysis in this study is limited to a specific grooved channel geometry corresponding to previous experiments. Future studies will explore a broader range of groove dimensions and configurations to enhance the generality of the findings. Although the current study does not aim to optimize a specific performance parameter, the observed wall shear stress and vortex intensity suggest potential targets for future optimization. Parameters such as groove geometry, Reynolds number, and boundary condition type could be varied systematically to identify configurations that enhance shear stress or mixing efficiency. A numerical design-of-experiments approach could be adopted in future work to support this goal.

Conflicts of Interest

The authors declare no conflicts of interest regarding the publication of this paper.

References

- [1] Ghaddar, N.K., Korczak, K.Z., Mikic, B.B. and Patera, A.T. (1986) Numerical Investigation of Incompressible Flow in Grooved Channels. Part 1. Stability and Self-Sustained Oscillations. *Journal of Fluid Mechanics*, **163**, 99-127.
<https://doi.org/10.1017/s0022112086002227>
- [2] Stroock, A.D., Dertinger, S.K.W., Ajdari, A., Mezić, I., Stone, H.A. and Whitesides, G.M. (2002) Chaotic Mixer for Microchannels. *Science*, **295**, 647-651.
<https://doi.org/10.1126/science.1066238>
- [3] Dewan, A. and Srivastava, P. (2015) A Review of Heat Transfer Enhancement through Flow Disruption in a Microchannel. *Journal of Thermal Science*, **24**, 203-

214. <https://doi.org/10.1007/s11630-015-0775-1>
- [4] Kwon, J. and Oh, J.H. (2018) Microfluidic Technology for Cell Manipulation. *Applied Sciences*, **8**, 992. <https://doi.org/10.3390/app8060992>
- [5] Nishimura, T., Nakagiri, H. and Kunitsugu, K. (1996) Flow Patterns and Wall Shear Stresses in Grooved Channels at Intermediate Reynolds Numbers. Effect of Groove Length. *Transactions of the Japan Society of Mechanical Engineers Series B*, **62**, 2106-2112. <https://doi.org/10.1299/kikaib.62.2106>
- [6] Nishimura, T., Kunitsugu, K. and Nakagiri, H. (1997) Fluid Mixing and Local Mass Transfer Characteristics in a Grooved Channel for Self-Sustained Oscillatory Flow. *Transactions of the Japan Society of Mechanical Engineers Series B*, **63**, 1707-1712. <https://doi.org/10.1299/kikaib.63.1707>
- [7] Kunitsugu, K. and Nishimura, T. (1999) Three-dimensional Numerical Simulation of Grooved Channel Flows. *Transactions of the Japan Society of Mechanical Engineers Series B*, **65**, 1893-1898. <https://doi.org/10.1299/kikaib.65.1893>
- [8] Nishimura, T. and Kunitsugu, K. (2001) Three-dimensionality of Grooved Channel Flows at Intermediate Reynolds Numbers. *Experiments in Fluids*, **31**, 34-44. <https://doi.org/10.1007/s003480000256>
- [9] Roberts, E.P.L. (1994) A Numerical and Experimental Study of Transition Processes in an Obstructed Channel Flow. *Journal of Fluid Mechanics*, **260**, 185-209. <https://doi.org/10.1017/s0022112094003484>
- [10] Mizushima, J., Okamoto, H. and Yamaguchi, H. (1996) Stability of Flow in a Channel with a Suddenly Expanded Part. *Physics of Fluids*, **8**, 2933-2942. <https://doi.org/10.1063/1.869072>
- [11] Takaoka, M., Sano, T., Yamamoto, H. and Mizushima, J. (2009) Convective Instability of Flow in a Symmetric Channel with Spatially Periodic Structures. *Physics of Fluids*, **21**, Article ID: 024105. <https://doi.org/10.1063/1.3067870>
- [12] Adachi, T. and Hasegawa, S. (2006) Transition of the Flow in a Symmetric Channel with Periodically Expanded Grooves. *Chemical Engineering Science*, **61**, 2721-2729. <https://doi.org/10.1016/j.ces.2005.11.042>
- [13] Kim, J., Moin, P. and Moser, R. (1987) Turbulence Statistics in Fully Developed Channel Flow at Low Reynolds Number. *Journal of Fluid Mechanics*, **177**, 133-166. <https://doi.org/10.1017/s0022112087000892>
- [14] Nishioka, M., Asai, M. and Suzuki, K. (1988) Randomization Process of Fluctuations in the Ribbon-Induced Transition of Plane Poiseuille Flow. *NAGARE*, **7**, 336-351. <https://doi.org/10.11426/nagare1982.7.336>
- [15] Alam, M.M.A., Hirano, T., Hayamizu, Y., Masuda, T., Hamada, T., Morita, S., *et al.* (2023) Micro T-Mixer with Baffles: Effect of Baffle Height and Setting Angle on Mixing. *Open Journal of Fluid Dynamics*, **13**, 206-215. <https://doi.org/10.4236/ojfd.2023.134015>
- [16] Masuda, T., Tagawa, T., Alam, M.M.A. and Hayamizu, Y. (2023) Structure of Periodic Flows through a Channel with a Suddenly Expanded and Contracted Part. *Open Journal of Fluid Dynamics*, **13**, 232-249. <https://doi.org/10.4236/ojfd.2023.135018>
- [17] Sanmiguel-Rojas, E. and Mullin, T. (2011) Finite-Amplitude Solutions in the Flow through a Sudden Expansion in a Circular Pipe. *Journal of Fluid Mechanics*, **691**, 201-213. <https://doi.org/10.1017/jfm.2011.469>
- [18] Sakurai, M. (2013) Three-Dimensional Structure of Laminar Flow through a Square Sudden Expansion Channel (Vortex Structure of the Recirculation Zone). *Transactions of the Japan Society of Mechanical Engineers Series B*, **79**, 317-327.

<https://doi.org/10.1299/kikaib.79.317>

- [19] Sakurai, M., Nakanishi, S. and Mochizuki, S. (2013) Three-Dimensional Structure of Laminar Flow through a Square Sudden Expansion Channel (Effect of Reynolds Number). *Transactions of the Japan Society of Mechanical Engineers Series B*, **79**, 1533-1545. <https://doi.org/10.1299/kikaib.79.1533>
- [20] Kunitsugu, K. and Nishimura, T. (2002) The Streamwise Development Process of Self-Sustained Oscillatory Flow in a Grooved Channel. *The Proceedings of Conference of Chugoku-Shikoku Branch*, **2002**, 55-56. <https://doi.org/10.1299/jsmeecs.2002.55>

Nomenclature

f^*	Frequency [s^{-1}]
H^*	Inlet channel height (=1 m)
p	Dimensionless pressure
Re	Reynolds number ($= \rho U^* H^* / \mu$)
St	Strouhal number ($= f^* H^* / U^*$)
t	Dimensionless time
U^*	Average inlet velocity in the main flow direction (=1 m/s)
\mathbf{u}	Dimensionless velocity ($= u_i = (u, v, w)$) ($i = 1, 2, 3$)
$\langle u_i \rangle$	Dimensionless velocity component ($= \langle u_i \rangle + u'_i$)
u_i	Dimensionless time-averaged velocity component
u'_i	Dimensionless time-varying velocity component
$u'_{i\text{RMS}}$	Root mean square (RMS) of u'_i
\mathbf{x}	Dimensionless spatial coordinate ($= x_i = (x, y, z)$) ($i = 1, 2, 3$)
μ	Viscosity [Pa·s]
ρ	Density [kg/m^3]
$\langle \tau_0 \rangle$	Time-averaged absolute value of dimensionless wall shear stress